

CERTIFICATE

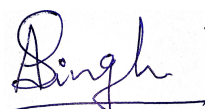
It is certified that the work contained in the thesis titled "**Novel Component Designs of Solar Energy Devices for Enhanced Thermal Performance**" by "**AJEET PRATAP SINGH**" has been carried out under my supervision and that this work has not been submitted elsewhere for a degree.

It is further certified that the student has fulfilled all the requirements of Comprehensive Examination, Candidacy and SOTA for the award of Ph.D. Degree.

Dr. Om Prakash Singh
Supervisor,
Associate Professor
Department of Mechanical Engineering
IIT(BHU) Varanasi

DECLARATION BY THE CANDIDATE

I, Ajeet Pratap Singh, certify that the work embodied in this thesis is my own bona fide work carried out by me under the supervision of Dr. Om Prakash Singh for a period of 3 years 11 months from July 2016 to June 2020 at IIT (BHU) Varanasi. The material contained in this thesis has not been submitted for the award of any other degree. I declare that I have faithfully acknowledged and given credits to the researchers wherever their works have been cited in my work in this thesis. I further declare that I have not willfully copied any others' work, paragraphs, text, data, results etc. reported in journals, books, magazines, reports, dissertations, theses, etc. or available at websites and have not included them in this thesis and have not cited as my own work.



Date :

Signature of the Student

Place:

(AJEET PRATAP SINGH)

CERTIFICATE BY THE SUPERVISOR(S)

It is certified that the above statement made by the student is correct to the best of my/our knowledge.

Dr. Om Prakash Singh
Supervisor

Signature of Head of Department/Coordinator of School

"SEAL OF THE DEPARTMENT/SCHOOL"

COPYRIGHT TRANSFER CERTIFICATE

Title of the Thesis : **Novel Component Designs of Solar Energy Devices for Enhanced Thermal Performance**

Name of the Student : **Ajeet Pratap Singh**

Copyright Transfer

The undersigned hereby assigns to the Institute of Technology (Banaras Hindu University) Varanasi all rights under copyright that may exist in and for the above thesis submitted for the award of the "*Doctor of Philosophy*".



Date :

Signature of the Student

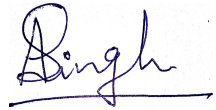
Place:

(AJEET PRATAP SINGH)

Note: However, the author may reproduce or authorize others to reproduce material extracted verbatim from the thesis or derivative of the thesis for author's personal use provided that the source and the Institute's copyright notice are indicated.

Acknowledgement

My research journey elevated my personality to the core. During this process, fore-mostly, I would like to thank my awe-inspiring supervisor Dr. Om Prakash Singh. He has brought out best in me by dealing calmly and intelligently, invigorating timely curiosity in me. His consistent enthusiasm and optimistic attitude towards research always uplifted me towards my work. His humble and polite disposition has been one of the greatest inspirations I ever had. I am truly indebted to him for his support, guidance and kindness. I was lucky to have attended his short term course on CFD during my first semester itself that helped me in understanding this complex subject of solar energy and its modeling techniques. It really helped in accelerating my research work. I also thank the faculty of Mechanical engineering department whose courses helped me immensely. Further, I find myself fortunate to have a circle of close friends: Sarvesh Yadav, Jitendra Kumar Goyal, Amit Kumar, Vivek Kumar, Sumit Kumar Singh, Sujeet Yadav, Sunil Kumar Yadav, who lightened the weight of the worst phases of my life and thus provided me the cushioned environment, which enhanced my creativity in my work. I end by acknowledging the basic source of my life energy, my family. I am thankful to them, whose struggle and immense love has encouraged me to come to the state of writing these lines. At this moment of accomplishment, I want to pay adoration to my mother, Smt Chanda Singh who has been the true inspiration for me and without her blessings, the completion of my thesis would not have been possible. I extend my gratitude to my father Shri Sukhendra Singh, my sister Mrs. Preeti Singh Rana, my brother-in-law Mr. Anuj Rana, my uncle Mr. M.Z.A. Siddiqui who have been a constant source of love, concern, support and strength all these years. Last but not least, I express my heartiest thanks to all of my well-wishers whose constant motivation enabled me to complete my thesis.



Ajeet Pratap Singh

Contents

Certificate	ii
Declaration	iii
Copyright	iv
Acknowledgement	v
Table of content	vi
List of figures	x
List of tables	xviii
Nomenclature	xxi
Abstract	xxv
1 Introduction	1
1.1 Energy resources: At a glance	1
1.2 Conventional solar devices: An outlook	2
1.3 Novel efficient designs	3
1.4 Objective of the thesis	5
1.5 Organization of the thesis	6
2 Novel designs of bell-mouth-converging collector integrated SCPP	9
2.1 Introduction	9
2.2 Description of problem	11
2.3 Experimental validation	13
2.4 Results and discussions	14
2.4.1 Bell-mouth orientation and design	14
2.4.2 Effect of 90° down bell-mouth with wedge shaped collector	15
2.4.3 Effect of wedge shape collector on chimney design	16
2.4.4 Combined effect of optimum bell-mouth, collector and chimney	20
2.4.5 Effect of large-scale model	23
2.5 Conclusion	23
3 Designs of collector-chimney of PV integrated SCPP	27
3.1 Introduction	27
3.2 Hybrid solar chimney model description	28
3.3 Numerical domain: discretization and modelling	31

3.3.1	Boundary conditions	31
3.3.2	Grid independence test	35
3.3.3	Experimental setup and validation	35
3.4	Results and discussions	36
3.4.1	Effect of divergent solar chimney	37
3.4.2	Converging collector passage with divergent chimney	40
3.5	Conclusion	46
4	Convex and concave collector designs of self-driven SAH	49
4.1	Introduction	49
4.2	Experimental set-up for validation	50
4.3	Objective and simulation methodology	52
4.3.1	New SAH designs	53
4.3.2	Selection of physics models and governing equations	53
4.3.3	Basic design details of geometry and parameters	54
4.3.4	Methodology of mesh generation and grid independent test	56
4.3.5	Boundary conditions and experimental validation	56
4.4	Results and discussions	58
4.4.1	Effect of concave and convex curved designs on thermal performance	58
4.5	Correlation development	64
4.5.1	Correlation development for concave designs of SAH	64
4.5.2	Correlation development for convex curved design	66
4.5.3	Percentage error	66
4.6	Conclusion	67
5	Bell-mouth integrated SAH for high flow rates	69
5.1	Introduction	69
5.2	Designs and the computational model	73
5.2.1	Design details and geometric parameters	74
5.2.2	Mesh generation and grid independence test	74
5.2.3	Boundary conditions	74
5.2.4	Necessary physics models and governing equations	75
5.2.4.1	Experimental set-up for validation	77
5.2.5	Pressure coefficient variation	77
5.3	Results and discussions	78
5.3.1	Effect of bell-mouth design (Flat + bell-mouth)	78
5.3.2	Effect of bell-mouth design with chimney (Flat + bell-mouth + chimney)	79
5.3.3	Why flow rate increases with the integration of bell-mouth design at inlet?	81
5.3.4	Energy conversion efficiency - Which is better: low-temperature high-flow or high-temperature low-flow SAH?	84
5.4	Correlation development	87
5.5	Conclusion	89
6	Bell-mouth with tapered collector for high temperature applications	91
6.1	Introduction	91
6.2	Description of the problem	93
6.2.1	Mesh generation and grid independency test	96
6.2.2	Boundary conditions	96
6.2.3	Non-dimensionless parameters and governing equations	97
6.3	Results and discussions	98
6.3.1	Effect of tapered flow channel on thermal performance	98
6.3.2	Hydraulic performance of tapered SAH with bell-mouth	101

6.4	Correlations development	103
6.5	Conclusion	107
7	Curved vs. flat collector designs: A comparative analysis	109
7.1	Introduction	109
7.2	Description of computational model	110
7.2.1	Basic design details of geometry and parameters	111
7.2.2	Methodology of mesh generation and grid independent test of computational domain	113
7.2.3	Boundary conditions	114
7.2.4	Selection of physics models and governing equations for solution	114
7.2.5	Global solar radiation and curved collector performance analysis	115
7.3	Thermal efficiency	115
7.4	Selection of turbulence model and validation of CFD model	116
7.5	Results and discussions	117
7.5.1	Effect of different geometries of SAH on heat transfer parameters and thermal efficiency	119
7.5.2	Effect of relative height and pitch ratio of corrugation	122
7.6	Correlation for Nusselt number and friction factor	127
7.7	Conclusions	130
8	Energy and exergy analysis of curved SAH with semi-down turbulators	133
8.1	Introduction	133
8.2	Numerical domain	134
8.2.1	Geometry specification and parametric details	134
8.2.2	Mesh description and grid independence of numerical model	136
8.2.3	Boundary conditions	137
8.2.4	Governing equations and physical terms	138
8.2.5	Assessment of magnitude of solar radiation received on curved SAH	139
8.3	Experimental validation of numerical model of curved SAH	139
8.4	Results and discussions	140
8.5	Exergy analysis	146
8.6	Development of Correlations	150
8.7	Conclusion	151
9	Curved vs. Flat SAH analysis under diverse ambient conditions	153
9.1	Introduction	153
9.2	The computational model	156
9.2.1	Design procedure for optimum curvature angle	156
9.2.2	Procedure for environmental wind effect study on curved SAH	156
9.2.3	Mesh generation and grid independence study	156
9.2.4	Grid independent test of a curved SAH for thermal performance	158
9.2.5	Grid independent test of a curved SAH for environmental wind condition	158
9.2.6	Boundary conditions	158
9.2.6.1	Boundary condition to find best curvature angle of a curved SAH	158
9.2.6.2	Boundary condition to study the effect of environmental wind condition	158
9.2.7	Physical models and sets of governing equations	159
9.2.8	Comparative assessment of globally received solar radiation on flat and curved SAH	160
9.3	Thermal efficiency	160
9.4	Validation of numerical model	161
9.4.1	Validation of curved solar air heater model	161
9.4.2	Validation of computational model of SAH under environmental wind conditions	161
9.5	Results and discussions	162
9.5.1	Curved Vs. Flat SAH: Thermal performance	162

9.5.1.1	Optimum curved angle	163
9.5.1.2	Performance comparison: curved vs. flat	163
9.5.2	Curved Vs. Flat SAH: Heat loss characteristics under environmental wind effect	166
9.5.2.1	Windward orientation	167
9.5.2.2	Leeward orientation	167
9.5.2.3	Performance under natural convection (standstill air environment)	169
9.5.3	Curved Vs. Flat SAH: Aerodynamic characteristics	172
9.5.3.1	Longitudinal pressure distribution	172
9.6	Conclusion	177
10	Conclusions and scope for future study	179
10.1	Conclusions	179
10.2	Major contributions from the thesis	184
10.3	Limitations of the present investigation	184
10.4	Suggestions for future research	185
	Bibliography	186
	Appendix A	197
	A	199
A.1	Grid independent test	199
A.1.1	Grid independent test of local velocity as parameter at different sections (refer Fig. A.2)	201
A.1.2	Grid independent test of temperature as parameter at different sections (refer Fig. A.3)	201
A.2	Time independent test	201
	B	203
	Appendix B	202
	Author's biodata	204

List of Figures

1.1	Solar energy in power generation application: (a) Solar chimney power plant [6], (b) SCPP key elements, (c) SCPP working. In this thesis, new design of a novel bell-mouth inlet has been proposed and investigated in detail. This new design has been investigated by integrating it to a solar chimney power plant and solar air heater.	2
1.2	Isometric view of high flow solar chimney power plant.	4
1.3	Schematic diagram of convex-concave buoyancy-driven solar air heater.	4
1.4	Schematic diagram of high flow solar air heater integrated with building.	5
1.5	Bell-mouth inlet opening retrofitted with converging collector of solar chimney power plant and solar air heater.	6
2.1	Schematic diagram of conventional solar chimney power plant: (a) Two-dimensional axisymmetric model; (b) Three-dimensional view of solar chimney model.	10
2.2	(a) Cross-sectional view of the new design of solar chimney power plant put on an elevated position. Notice the design of bell-shaped inlet integrated with the wedge shaped (convergent) collector with divergent chimney. The parametric range bell-mouth design ratio $h/R = 0.4 - 1$, taper ratio $TR = 1.2 - 3$ and $CORR = 1 - 5$; Cross-section of the three-dimensional view of SCPP configuration comprises (b) horizontally placed bell-mouth, and (c) 90° downward bell-mouth inlet- integrated with wedge shape collector-divergent chimney.	12
2.3	(a) Experimental prototype of solar chimney of the literature Ghalamchi et al., 2016 [52]. Comparison of the (b) velocity and (c) temperature profiles using numerical data with the experimental data of the literature Ghalamchi et al., 2016 [52].	14
2.4	Effect on velocity variation at inlet of the collector when integrated with bell-mouth design inlet in conventional SCPP. Bell-mouth with 90° down configuration shows flatter profile across the inlet. Bell-mouth design parameters are: $R = 0.14$ and $h/R = 0.57$. Variation was measured in the marked section 1-1 as shown in inset figure.	15
2.5	Flow velocity variation along collector radius for the taper ratio TR in the range 1 – 3 and the best TR i.e. 3 with the best performing bell-mouth design. Measured location 1-1 to 2-2 is shown in inset figure.	16
2.6	Temperature variation along collector radius for the taper ratio TR in the range 1 – 3 and the best TR i.e. 3 with the best performing bell-mouth design. Measured location 1-1 to 2-2 is shown in inset figure.	17
2.7	Air pressure distribution along chimney height for taper ratio TR in the range 1 – 3 and best TR = 3 with the optimum bell-mouth.	17
2.8	Velocity at the collector outlet for the combination: the best wedge shape collector having $TR = 3$ integrated with different divergent chimney for the CORR range 1.5 – 5.	18
2.9	Velocity variation along the collector radius of the solar chimney for the combination: the best wedge shape collector having $TR = 3$ integrated with different divergent chimney for the CORR range 1.5 – 5. Measured location 1-1 to 2-2 is shown in inset figure.	19

2.10	Air temperature distribution along the collector radius of the solar chimney for the combination: the best wedge shape collector having $TR = 3$ integrated with different divergent chimney for the CORR range 1.5 – 5 . Measured location 1-1 to 2-2 is shown in inset figure.	20
2.11	Velocity variation at the chimney outlet of the solar chimney for the combination: the best wedge shape collector having $TR = 3$ integrated with different divergent chimney for the CORR range 1.5 – 5. The enlarged value of higher CORR values 4, 4.5, and 5 with velocity contours shows how velocity fluctuates across the exit length due to recirculation zone formation.	21
2.12	(a) Velocity distribution along chimney height from section 3-3 to 4-4 (inset shown) for the combination: the best wedge shape collector having $TR = 3$ integrated with different divergent chimney for the CORR range 1.5 – 5, (b) Enlarged view of velocity variation at higher CORR clearly depicting significant fluctuations in velocity magnitude due to adverse pressure gradient developed along the chimney height.	22
2.13	Air pressure distribution along chimney height for the system with optimum wedge shape collector ($TR = 3$) integrated with different divergent chimney having CORR range 1.5 – 5. Note that $TR = 3$ an $CORR = 2$ exhibits higher pressure difference thereby enhancing driving potential.	23
2.14	Velocity variation along the collector radii for the best solar chimney design for each discussed cases: 1. Only wedge shape collector, 2. Only divergent chimney, 3. Wedge shape collector integrated with divergent chimney, and 4. Bell-mouth opening at the inlet of wedge shape collector integrated with divergent chimney. Measured location 1-1 to 2-2 is shown in inset figure.	24
2.15	Static pressure recovery variation along the chimney height for the best configuration from each case: 1. Only divergent chimney, 2. Wedge shape collector integrated with divergent chimney, and 3. Bell-mouth opening at the inlet of wedge shape collector integrated with divergent chimney. Measured location 3-3 to 4-4 is shown in inset figure. Note that the higher static pressure recovery along the chimney height is observed with the integration of bell-mouth at the inlet.	24
2.16	Contour plot of static pressure recovery have shown to compare the best solar chimney design comprised of best taper collector, divergent chimney, and bell-mouth shaped collector inlet i.e. $TR = 3$, $CORR = 2$ and optimum BM, respectively, to compare best design results with the conventional solar chimney design.	25
3.1	Schematic diagram of a new hybrid solar chimney power plant: (a) Two-dimensional axisymmetric model; (b) Three-dimensional view of computer aided design (CAD) model after 360° rotation. Enlarged view of the PV panel is shown as inset. Sections are marked with numbers where performance data is reported. Design changes in flow channel is shown in Fig. 2.	31
3.2	New designs of the hybrid solar chimney power plant with range of taper ratio $TR = 0.34 - 0.83$ and $CORR = 1 - 5$. (a) Conventional design; (b) Conventional collector with divergent chimney; (c) Tapered collector with conventional chimney; (d) Tapered collector with divergent chimney.	32
3.3	Meshed computational domain of HSCPP design with enlarged view of different zones.	33
3.4	Grid independence test for different number of elements shown for the conventional design of solar chimney having dimensions identical to the experimental design of the literature [52].	35
3.5	(a) Solar chimney experimental set-up [18]. Comparison of (b) velocity and (c) temperature profile obtained from numerical model with the experimental data of the literature [52].	36
3.6	Velocity profile along the collector radius for different CORR values of divergent chimney. Variation is shown between 0-0.6 m where significant difference is seen. Zero radii is located at the center of chimney. CORR =1 corresponds to conventional chimney.	37
3.7	Local variation of PV panel efficiency along the collector radius for different CORR range 1-5 of divergent chimney. CORR =1 corresponds to conventional HSCPP.	38
3.8	Velocity variation along the height of the chimney for different CORR range 1-5 of divergent chimney. CORR =1 denote conventional HSCPP.	38
3.9	Static pressure variation along the height of the chimney for different CORR range 1-5 of divergent chimney. CORR =1 denote conventional HSCPP.	39

3.10	Velocity variation at the chimney outlet i.e. at section 4-4 for different CORR range 1-5 of the divergent chimney. At higher CORR, reverse flow is seen (see inset). CORR =1 denote conventional HSCPP.	40
3.11	Total pressure variation at the chimney outlet i.e. section 4-4 for different CORR range 1-5 of divergent chimney.	41
3.12	Velocity variation along the collector radii for different taper ratio (TR) range 0.34-1 with conventional cylindrical and divergent chimney. In all cases, the opening inlet height H_2 has been kept constant.	41
3.13	Efficiency variation of the PV panel along the collector radii for different taper ratio (TR) range 0.34-1 combined with divergent chimney.	42
3.14	Velocity contours for various designs of HSCPP.	43
3.15	Pressure contours for various designs of HSCPP.	44
3.16	Turbulent kinetic energy for various designs of HSCPP.	45
3.17	HSCPP designs categorization based on percentage gain in photovoltaic electrical conversion efficiency compared to the conventional HSCPP design.	46
4.1	Experimental set up of a conventional flat plate natural convection solar air heater (Gilani et al., 2017): (a) chimney, solar air heater and data collection unit, (b) side view showing the flow direction and location of measuring instruments (1- chimney, 2- double glaze glass top cover, 3- wind protector, 4- probe thermocouple, 5- wire thermocouple, 6- absorber plate, 7- hot wire anemometer, 8- solarimeter).	50
4.2	The natural convective flat SAH at an angle (θ) of 45° with respect to horizontal.	51
4.3	The natural convective concave curved SAH inclined at an angle (θ) of 45° with respect to horizontal plane, connected to a vertical chimney. Effect of curvature angle on thermo-hydraulic performance has been investigated.	52
4.4	The natural convective convex curved SAH inclined at an angle (θ) of 45° with respect to horizontal plane, connected to a vertical chimney. Effect of curvature angle on thermo-hydraulic performance has been investigated.	53
4.5	Computational mesh domain of the flat natural convective SAH. Boundary layer mesh is shown in the magnified views.	55
4.6	Validation of computation flow model with the experimental data of the literature (Gilani et al., 2017).	57
4.7	Variation of TER of: (a) concave curved natural convective SAH; (b) convex curved natural convective SAH, for six different curvature angle in the range of 25° - 50°	59
4.8	variation of HTEF of: (a) concave curved natural convective SAH; (b) convex curved natural convective SAH, for six different curvature angle in the range of 25° - 50°	59
4.9	Variation of Nu w.r.t. temperature factor, $\frac{(T_o-T_i)}{T}$, of flat and different curvature angle (30° , 40° and 50°) of: (a) concave curved natural convective SAH; (b) convex curved natural convective SAH, at different values of constant absorber heat flux in the range 500 - 1100 W/m^2	60
4.10	The plot shows effectiveness of concave and convex curved and flat- flow passage of natural convective SAH with respect to different values of constant absorber heat flux.	61
4.11	Shows the variation of Nu vs. Ra of concave and convex curved- SAH at all value of heat flux in the range of 500 - 800 W/m^2	61
4.12	The temperature and velocity contours have been shown for convex SAH having best curvature angle 30° at constant absorber heat flux of 800 W/m^2 . (a) Temperature contours; Velocity contours at (b) chimney outlet, (c) SAH exit and (d) SAH inlet section. Similar contours were observed for other curvature angles.	62
4.13	The temperature and velocity contours have been shown for concave SAH having best curvature angle 40° at constant absorber heat flux of 800 W/m^2 . (a) Temperature contours; Velocity contours at (b) chimney outlet, (c) SAH exit and (d) SAH inlet section. Similar contours were observed for other curvature angles.	63

4.14	Plot of $\ln(Nu)$ versus $\ln(Ra \cos\theta)$ of concave curved natural convective SAH.	65
4.15	Variation of $\ln(A_o)$ versus $\ln(\phi)$ of concave curved natural convective SAH.	65
4.16	Comparison between values of Nusselt number correlation (Nu_{corr}) and Nusselt number CFD (Nu_{CFD}) of concave curved natural convective SAH.	66
4.17	Comparison between values of Nusselt number correlation (Nu_{corr}) and Nusselt number CFD (Nu_{CFD}) of convex curved natural convective SAH.	66
5.1	Solar dryer integrated with conventional flat plate natural convection solar air heater having rectangular cross-sectional inlet design [121].	70
5.2	(a) Flat plate natural convection SAH integrated with bell-mouth at the SAH inlet and chimney at the SAH exit; (b) Enlarged view of inlet section.	74
5.3	Computational mesh domain of the natural convection SAH integrated with bell-mouth and chimney. Boundary layer mesh is shown in the magnified views.	75
5.4	Validation of the present numerical model with experimental and numerical results of the literature [34]. The temperature profiles across the channel width at $H=7.8$ m have been compared.	77
5.5	Variation of local air flow velocity at the inlet integrated with different shapes of bell-mouth (h/R in the range 0.1-0.6) at absorber heat flux of 1000 W/m^2 . Measured location (0 mm -102 mm) has been marked in the inset.	79
5.6	Variation of local pressure coefficient (C_p) at the inlet integrated with different shape of bell-mouth (h/R in the range 0.1-0.6) at absorber heat flux of 1000 W/m^2 . Measured location (0 mm -102 mm) has been marked in the inset.	80
5.7	Variation of Nusselt number of SAH integrated with different shape of bell-mouth (h/R in the range 0.1 – 0.6) with Rayleigh number.	80
5.8	Variation of mass flow rate when integrated with different shape of bell-mouth (see legend) with chimney at different solar insolation.	81
5.9	Variation of pressure coefficient (C_p) at the inlet of SAH integrated with different shape of bell-mouth with chimney, at absorber heat flux of 1000 W/m^2	82
5.10	Variation of local air flow velocity at the inlet of SAH integrated with different shape of bell-mouth with chimney at absorber heat flux of 1000 W/m^2	82
5.11	Variation of Nusselt number with Rayleigh numbers for various designs (see legend).	83
5.12	Schematic diagram of flow patterns when fluid flows at the inlet of SAH duct with two different inlet designs: (a) Flat rectangular inlet, (b) bell-mouth shape inlet. Notice how the size of vena contracta are different for flat and bell-mouth shape inlet. The vorticity contours when air flows through the SAH duct having: (c) flat rectangular inlet, (d) bell-mouth shape ($h/R = 0.6$, $R = 50 \text{ mm}$) inlet. The velocity contours when air flows through the SAH duct having: (e) flat rectangular inlet, (f) bell-mouth shape ($h/R = 0.6$, $R = 50 \text{ mm}$) inlet.	85
5.13	High flow SAH integrated with a space having dimensions $L = 10\text{m}$, $W = 10\text{m}$ and $H = 10\text{m}$ for heating in cold climatic condition.	86
5.14	Schematic representation of various naturally driven solar air heaters configuration based on their mass flow rates. The mass flow rate values mentioned are for the heat flux $500\text{-}1100 \text{ W/m}^2$	87
5.15	Plot of $\ln(Nu)$ versus $\ln(Ra \cos\theta)$ of flat natural convection SAH having bell-mouth shape inlet.	88
5.16	Comparison between values of Nu_{corr} and Nu_{CFD} of flat natural convection SAH having bell-mouth shape inlet.	89
6.1	Tapered SAH with bell-mouth integrated with building for space heating and ventilation.	92
6.2	Conventional design of natural convection SAH having parallel flow passage at an inclination angle (θ) of 45°	93
6.3	Natural convection tapered SAH inclined at $\theta = 45^\circ$, integrated with a vertical chimney. Note that while the dimension of inlet passage is kept constant, outlet width of SAH and chimney was varied. The dimensions are: (a) $H_1 = 102\text{mm}$, $H_2 = 50\text{mm}$ & $t_c = 60\text{mm}$ (b) $H_1 = 102\text{mm}$, $H_2 = 60\text{mm}$ & $t_c = 70\text{mm}$, (c) $H_1 = 102\text{mm}$, $H_2 = 70\text{mm}$ & $t_c = 80\text{mm}$, (d) $H_1 = 102\text{mm}$, $H_2 = 80\text{mm}$ & $t_c = 90\text{mm}$, (e) $H_1 = 102\text{mm}$, $H_2 = 90\text{mm}$ & $t_c = 100\text{mm}$	94

6.4	Natural convective tapered SAH united with bell-mouth shape inlet. The enlarged view of bell-mouth inlet opening is shown on the right. Each design of tapered SAH shown in Fig. 6.3 are individually analysed to understand the influence of bell shape opening on the performance of the device.	95
6.5	Meshed geometry of the numerical domain of tapered natural convection solar air heater. Magnified view shows boundary layer mesh near the heated absorber plate and chimney.	96
6.6	Variation of thermal enhancement ratio (TER) with heat flux (q) for tapered flow passage natural convection SAH.	99
6.7	Variation of Nusselt number, Nu with Rayleigh number, Ra for tapered flow passage natural convective SAH of rectangular cross-sectional shape inlet.	100
6.8	Variation of mass flow rate for tapered flow passage SAH with rectangular cross-sectional shape inlet for solar insolation range 500-1100 W/m ²	100
6.9	Variation of thermal effectiveness of flat tapered natural convection SAH vs. Rayleigh number for the range of $q = 500 - 1100$ W/m ²	102
6.10	Mass flow rate variation for various bell-mouth shape inlet designs integrated with conventional SAH for the range of absorber heat flux 500 – 1100 W/m ²	102
6.11	Mass flow rate variation with Rayleigh number for tapered SAH integrated with bell-mouth design inlet.	103
6.12	Variation of mass enhancement ratio (MER) of tapered SAH with bell-mouth shape inlet compared to the rectangular cross-sectional inlet of conventional SAH for the heat flux range 500 – 1100 W/m ²	104
6.13	Plot of Nu vs. Ra variation for tapered SAH having bell-mouth design integrated at the inlet for the range of heat flux 500-1100 W/m ²	104
6.14	Velocity contour plot at heat flux 800 W/m ² : (a) tapered SAH (taper ratio = 0.69) integrated with bell-mouth ($h/R = 0.3$); (b) conventional SAH (parallel flow passage).	105
6.15	$\ln(\text{Nu})$ vs. $\ln(\text{Ra} \cos\theta)$ of tapered natural convection solar air heater.	106
6.16	Plot of $\ln(A_o)$ vs. $\ln(H_2/H_1)$ of tapered natural convection SAH.	106
6.17	Variation of Nusselt number obtained by correlation (Nu_{corr}) and simulation (Nu_{CFD}) of tapered natural convection SAH.	107
7.1	(a) Experimental setup [1]; (b) Solid geometry of curved plate SAH.	111
7.2	(i) Two-dimensional solid geometry of various curved SAH design. (a) FPSP, (b) FPDP, (c) CPSP, (d) CPDP, (e) CPSCSP (P=15 mm), (f) CPSCSP (P=10 mm) and its magnified view of corrugation, (g) CPVCSP (P=15 mm), and (h) CPVCSP (P=10 mm) and its magnified view of corrugation; (ii) Air flow passage in the duct of curved SAH. (a) Partial side view of single pass flow of curved SAH, (b) Partial side view of double pass flow of curved SAH, (c) Partial side view of semicircular corrugation, (d) Partial side view of V-groove corrugation, (e) Front view of curved SAH.	112
7.3	Partial view of mesh refinement region near the absorber surface and bottom wall: (a) CPVCSP-SAH and (b) CPSCSP-SAH.	113
7.4	Comparison of outlet air temperature (T_o) of different turbulence models with experimental data at different values of mass flow rate i.e. 0.0172, 0.029, 0.0472 kg/sm ²	117
7.5	Variation in thermal efficiency at mass flow rate of 0.0172, 0.029 and 0.0472 kg/sm ² under constant absorber heat flux of 800 W/m ²	118
7.6	Variation in thermal efficiency at mass flow rate of 0.0172, 0.029 and 0.0472 kg/sm ² under constant absorber heat flux of 800 W/m ²	118
7.7	Air outlet temperature (T_o) variation of FPSP, FPDP, CPSP & CPDP SAH w.r.t. absorber heat flux at constant mass flow rate of 0.0472 kg/sm ²	119
7.8	Thermal efficiency of FPSP, FPDP, CPSP & CPDP SAH w.r.t. mass flow rate at constant absorber heat flux of 800 W/m ²	120

7.9	Thermal efficiency variation for different geometries of SAH at different mass flow rate values of 0.0172, 0.029, and 0.0472 kg/sm ²	120
7.10	Percentage variation of air outlet temperature (T_o) for different geometries of SAH w.r.t. FPSP and CPSP at different values of absorber heat flux.	121
7.11	Percentage variation of thermal efficiency for different geometries of SAH w.r.t. temperature parameter $\frac{(T_o-T_i)}{I}$	122
7.12	Nusselt number variation for different geometries of SAH at each value of mass flow rate i.e. 0.0172, 0.029 and 0.0472 kg/sm ² , respectively.	123
7.13	Percentage variation of Nusselt number for different geometries of SAH w.r.t. FPSP and CPSP at different values of absorber heat flux.	123
7.14	Pressure drop variation for different geometries of SAH at each value of mass flow rate i.e. 0.0172, 0.029 and 0.0472 kg/sm ² , respectively.	124
7.15	Friction factor (f) variation w.r.t. mass flow rate values of 0.0172, 0.029, and 0.0472 kg/sm ²	124
7.16	(a) and (b) Partial side view of secondary flow vortices formation near the sharp edge of V-grooves having different pitch values of the absorber plate. (a) Velocity contour at the sharp vortex of V-grooves having 10 mm pitch of curved SAH, (b) Velocity contour at the sharp vortex of V-grooves having 15 mm pitch of curved SAH.	125
7.17	(a), (b) and (c) Total pressure coefficient for different geometries of curved SAH at mass flow rate of 0.0472 kg/sm ² . (a) Total pressure coefficient of CPSP SAH, (b) Total pressure coefficient of CPVCSP SAH ($P/e = 1.25$), (c) Total pressure coefficient of CPVCSP SAH ($P/e = 0.834$).	126
7.18	Turbulent kinetic energy contours of V-corrugated SAH at mass flow rate of 0.0472 kg/sm ² . (a) Turbulent kinetic energy of CPVCSP SAH ($P/e = 1.25$), (b) Turbulent kinetic energy of CPVCSP SAH ($P/e = 0.834$).	127
7.19	Plot of $\ln(\text{Nu})$ versus $\ln(\text{Re})$ of curved SAH having corrugated absorber plate.	128
7.20	Plot of $\ln(\text{Ao})$ versus $\ln(P/e)$ of curved SAH having corrugated absorber plate.	129
7.21	Plot of $\ln(\text{Bo})$ versus $\ln(e/H)$ of curved SAH having corrugated absorber plate.	129
7.22	Comparison between values of Nusselt number correlation (Nu_{cor}) and Nusselt number CFD (Nu_{CFD}) of curved SAH having corrugated absorber plate.	130
7.23	Comparison between values of friction factor correlation (f_{cor}) and friction factor CFD (f_{CFD}) of curved SAH having corrugated absorber plate.	131
8.1	Previous investigations based on solar air heater straight flow channel equipped with various shape of ribs in two different arrangements of ribbed absorber plate: (a) down ribs and (b) up/bottom ribs.	135
8.2	Geometry of a curved SAH having 25° curvature angle with the half-triangular (i.e. (i)) grooved absorber plate. The three different shape of ribs have been considered in the study are shown: (i) half-triangular, (ii) half-trapezoidal and (iii) quarter-circle, and analyzed individually to investigate thermo-hydraulic performance.	136
8.3	Mesh of the computational flow domain of curved SAH equipped with half-triangular shape ribs.	137
8.4	Outlet air temperature variation (T_o) with solar radiation intensity (I) at the mass flow rate of 0.0172 kg/s.m ²	140
8.5	Variation of temperature factor, $\frac{(T_o-T_i)}{I}$, of curved SAH equipped with different shape of ribs for Re in the range 11000-15000, at $q = 1000 \text{ W/m}^2$	141
8.6	Shows Nusselt number variation for different shapes of ribs for Re in the range 11000 – 15000, at $q = 1000 \text{ W/m}^2$	142
8.7	Flow velocity profiles of (a) curved smooth SAH and (b) flat smooth SAH at different axial locations along the duct height for Re in the range 11000 at $q = 1000 \text{ W/m}^2$	143
8.8	Friction factor variation for various shape of ribs for Re in the range 11000 – 15000, at $q = 1000 \text{ W/m}^2$	144
8.9	Thermohydraulic performance $\frac{(T_o-T_i)}{I}/f$, variation of different shape of ribs for Re in the range 11000 – 15000, at $q = 1000 \text{ W/m}^2$	144

8.10	Plot ($\frac{Nu}{\Delta P}$) vs. Re at $q = 1000 \text{ W/m}^2$ for various shape of ribs.	145
8.11	Variation of effectiveness of different shape of ribs with Re , at $q = 1000 \text{ W/m}^2$	145
8.12	Demonstrates variation of exergy recovery of curved and flat- SAH devices with respect to temperature factor of different shape of ribs for the range of Re 11000-15000, at $q = 1000 \text{ W/m}^2$	147
8.13	Demonstrates second law efficiency (η_{II}) variation of curved and flat- SAH devices with respect to temperature factor of different shape of ribs for the range of Re 11000 – 15000, at $q = 1000 \text{ W/m}^2$	148
8.14	(a) Vorticity, (b) turbulent dissipation rate and (c) temperature contours of the curved SAH equipped with quarter-circle ribs having $e_r/H = 0.125$ and $e_r/b_r=1$, half-trapezoidal ribs having $e_{tp}/H= 0.125$ and half-triangular ribs having $e_t/H = 0.125$ and $e_t/b_t =1$, respectively, for the Reynolds number of 11000, at $q = 1000 \text{ W/m}^2$; (d) and (e) showing the Nusselt number and temperature contours at various regions for the best performing half-trapezoidal ribs at the middle section of curved and flat SAH, respectively.	149
8.15	Plot of Nusselt number along the absorber length of best performing curved half-trapezoidal ribbed SAH having $e_{tp}/H= 0.125$ and smooth curved SAH for the Reynolds number 11000, at $q = 1000 \text{ W/m}^2$. Magnified views of velocity contours are also shown at different axial locations along the duct height. Notice how Nu continuously decrease in both the cases, however, Nu shoots up at the location of ribs.	150
8.16	Variation of $\ln A_o$ vs. $\ln \frac{e_r}{H}$	151
8.17	Comparison of Nusselt number values obtained numerically and derived correlation.	151
9.1	(a) Experimental set up [102]; (b) Experimental set up [158].	154
9.2	Design description of the curved SAH model. (a) solar insolation on a curved SAH at different angles, (b) dimensions of the curved SAH geometry, (c) wind direction representation w.r.t. tilt angle (θ) of SAH.	155
9.3	Design description of various geometric parameters to determine the effects of environmental wind conditions on SAH. (a) wind tunnel design specification, (b) windward orientation, (c) leeward orientation.	157
9.4	Mesh of computational flow domain of the curved SAH in a wind tunnel.	157
9.5	(a) Variation of outlet air temperature (T_o) of a curved plate SAH w.r.t. constant value of absorber heat flux (W/m^2) at mass flow rate $m = 0.0172 \text{ kg/s.m}^2$; (b) Variation in thermal efficiency at mass flow rate in the range of 0.0172-0.0472 kg/s.m^2 at constant heat flux of 800 W/m^2	161
9.6	Nusselt number variation of CFD model (designed dimensionally same as the experimental set up [13]) and literature [13] (see Fig. 9.1(b)) w.r.t. different tilt angles (ϑ) of the flat solar collector.	162
9.7	Major variation of T_o of curved SAH for different curvature angle when the absorber surface exposed to constant heat flux of 800 W/m^2 , at fixed value of mass flow rate i.e. 0.0472 kg/sm^2	163
9.8	(a), (b), (c), and (d) shows the variation of outlet air temperature with time when solar radiation inclination angle in range of $\theta_i=0^\circ -60^\circ$ of curved SAH (25° curvature angle) at different values of mass flow rate (i.e. 0.0172, 0.029 and 0.0472 kg/sm^2).	164
9.9	(a), (b), (c), and (d) shows the variation of heat transfer enhancement factor (EF) with time when solar radiation inclination angle in range of $\theta_i = 0^\circ - 60^\circ$ of curved SAH (25° curvature angle) at different values of mass flow rate (i.e. 0.0172, 0.029 and 0.0472 kg/sm^2).	165
9.10	Nu variation for the tilt angle $\theta = 0^\circ$ of curved and flat SAH at wind velocity of 3 m/s.	166
9.11	Nusselt number variation for tilt angle $\theta = 15^\circ$ of curved and flat SAH at wind velocity of 3 m/s in windward position.	167
9.12	Nusselt number variation for tilt angle $\theta = 30^\circ$ of curved and flat SAH at wind velocity of 3 m/s in windward position.	168
9.13	Nusselt number variation for tilt angle $\theta = 45^\circ$ of curved and flat SAH at wind velocity of 3 m/s in windward position.	168

9.14	Nusselt number variation for tilt angle $\theta = 60^\circ$ of curved and flat SAH at wind velocity of 3 m/s in windward position.	169
9.15	Velocity contours: (a) curved and (b) flat SAH. (c) Nusselt number variation for tilt angle $\theta = 15^\circ$ of curved and flat SAH at wind velocity of 3 m/s in leeward position.	170
9.16	Velocity contours: (a) curved and (b) flat SAH. (c) Nusselt number variation for tilt angle $\theta = 30^\circ$ of curved and flat SAH at wind velocity of 3 m/s in leeward position.	170
9.17	Velocity contours: (a) curved and (b) flat SAH. (c) Nusselt number variation for tilt angle $\theta = 45^\circ$ of curved and flat SAH at wind velocity of 3 m/s in leeward position.	171
9.18	Velocity contours: (a) curved and (b) flat SAH. (c) Nusselt number variation for tilt angle $\theta = 60^\circ$ of curved and flat SAH at wind velocity of 3 m/s in leeward position.	171
9.19	Average Nusselt number variation of curved and flat SAH at constant absorber heat flux for various tilt angle under natural convection condition.	172
9.20	Velocity contours of curved and flat SAH at various tilt angle ($\theta = 15^\circ, 30^\circ, 45^\circ$ and 60°) under natural convection condition.	173
9.21	Pressure coefficient (C_P) variation at the top and bottom surface of flat and curved SAH for various SAH tilt angle at wind velocity (v) of 4 m/s: (a) flat SAH at windward position (b) curved SAH at windward position; (c) flat SAH at leeward position; (d) curved SAH at leeward position. Insert in the figures shows wind direction and net force acting on the SAH, F_L denotes net lift force and F_D denotes net downward force.	174
A.1	Flat natural convection SAH with four different sections placed longitudinally one after the other across the flow channel.	199
A.2	The velocity profiles at four different sections have been shown for flat natural convection SAH for different number of mesh elements.	200
A.3	The temperature profiles at four different sections have been shown for flat natural convection SAH for different number of mesh elements.	200
B.1	Trend variation of $\ln(\text{Nu})$ versus $\ln(\text{Re})$ for SAH having curved design equipped with quarter-circle ribs.	203

List of Tables

2.1	Design parameters of solar chimney [52].	11
2.2	Performance data of various SCPP designs. Note that $TR=1$ and $CORR = 1$ represent conventional solar chimney power plant.	18
3.2	Design parameters of solar chimney [52].	30
3.3	Polycrystalline silicon PV module characteristics [60].	31
3.4	Boundary conditions	34
3.5	Ambient fluid properties at the collector inlet of HSCPP at ambient temperature of 300 K.	34
3.6	Performance data of various HSCPP designs. Note that $TR = 1$ and $CORR = 1$ represent conventional hybrid solar chimney power plant.	43
4.1	Curvature angle and boundary conditions.	55
4.2	Details of grid independent test.	56
4.3	Thermo-physical properties of air at 298 K at the inlet of SAH.	57
4.4	Average effectiveness values for convex, concave and flat natural convective SAH at constant absorber heat flux for range 500-1100 W/m ²	60
4.5	(ΔP) and (NuP) values for convex and concave curved- natural convection SAH at constant absorber heat flux of 800 W/m ²	64
5.2	Range of geometric and operating parameters.	73
5.3	Air properties at the inlet of SAH at ambient temperature of 300 K.	75
6.1	Operating and geometrical parameters.	95
6.2	At the SAH inlet ambient air properties at 298 K are:	97
6.3	(ΔP) and (NuP) values for tapered - natural convective SAH without bell-mouth at $q = 800$ W/m ²	101
7.1	Range of parameters.	111
7.2	Detail of grid independent test.	114
7.3	Thermo-physical properties of air at 300 K.	114
7.4	EAF efficiency augmentation factor.	121
8.1	Description of design and flow parameters.	136
8.2	Grid independence test.	137
8.3	Air properties at 300 K.	138
9.1	Range of parameters.	156
9.2	Grid independent test of a curved SAH.	158
9.3	Grid independent test of environmental wind effect on the curved SAH.	158
9.4	Thermo-physical properties of air at 300 K.	159
9.5	Range of CP for curved and flat SAH in windward position.	175

9.6	Range of C_P for curved and flat SAH in leeward position.	176
A.1	Grid independent test details	200
A.2	Time step test details. Three times steps has been considered: time t , $t/2$ and $2t$	201

Nomenclature

A_c	Collector area (m ²)
A_p	Surface area of the absorber plate (m ²)
b_r	Width of quarter-circle groove (m)
b_t	Width of half-triangular groove (m)
b_{tp}	Top width of half-trapezoidal groove (m)
b_{tpd}	Bottom width of half-trapezoidal groove (m)
C_p	Pressure coefficient
ΔC_P	Streamwise differential pressure coefficient, $\frac{(P_t - P_b)}{1/2 \rho V_\infty^2}$
C_{tp}	Total pressure coefficient
D_e	Equivalent diameter (m)
D_H	Hydraulic diameter (m)
D_n	Dean number
e_r	Quarter-circle groove height (m)
e_r/H	Relative quarter-circle groove height ratio
e_t	Half-triangular groove height (m)
e_t/H	Relative half-triangular groove height ratio
e_{tp}	Half-trapezoidal groove height (m)
e_{tp}/H	Relative half-trapezoidal groove height ratio
e_v/H	Relative V-groove height ratio
f	Friction factor
h	Convection heat transfer coefficient (W m ⁻² K ⁻¹)
H	Duct opening of solar air heater flow passage (m)
H_1	Width of the duct inlet opening (m)
H_2	Width of the duct outlet opening (m)
H_c	Chimney height (m)
h/R	Bell-mouth design ratio
I	Solar irradiance (W m ⁻²)
k_a	Thermal conductivity of air (W m ⁻¹ K ⁻¹)
k_g	Thermal conductivity of glass (W m ⁻¹ K ⁻¹)
k_i	Thermal conductivity of insulation (W m ⁻¹ K ⁻¹)
L	Solar air heater duct length (m)
L_c	Characteristic length (m)
\dot{m}	Mass flow rate (kg s ⁻¹)
Nu	Nusselt number
P	Pitch of grooves (m)
P/e_t	Relative pitch ratio of half-triangular groove
P/e_{tp}	Relative pitch ratio of half-trapezoidal groove
P/e_r	Relative pitch ratio of quarter-circle groove
P/e_v	Relative pitch ratio of V-groove
ΔP	Pressure drop (N m ⁻¹)
Pr	Prandtl number

P_s	Static pressure at the location (Pa)
P_t	Total pressure at the location (Pa)
q	Heat flux (W m^{-2})
Q_u	Useful heat gain (J)
R	Bell-mouth curvature radius (m)
Ra	Rayleigh number
R_c	Curvature radius of the curved SAH geometry (m)
R_{ci}	Chimney inlet radius (m)
R_{co}	Chimney outlet radius (m)
Re	Reynolds number
t_c	Thickness of opening of the chimney (m)
T_i	Inlet temperature of air (K)
t_i	Thickness of the insulation (m)
T_o	Outlet temperature of air (K)
T_s or T_{pm}	Mean temperature of absorber plate (K)
V	Flow velocity (m s^{-1})
W	Width of the solar air heater duct (m)

Greek symbols

ρ	Density of air (kg m^{-3})
ρ_g	Ground reflectance
μ	Dynamic viscosity of air (N s m^{-2})
ε	Thermal effectiveness
ϵ	Emissivity
α	Absorptivity
τ	Glass plate transmissivity
ϕ	Curvature angle of curved solar air heater ($^\circ$)
η	Efficiency
$\tau\alpha$	Transmittance-absorbent product of glass cover
θ_z	Solar zenith angle ($^\circ$)
γ	Surface azimuth angle ($^\circ$)
γ_s	Solar azimuth angle ($^\circ$)

Subscripts

a	Ambient condition
∞	Freestream condition
o	Initial condition
g	Glass cover
i	Inlet section
o	Outlet section
p	Absorber plate
th	Thermal
θ	Angle of solar air heater w.r.t. horizontal plane ($^\circ$)
θ_i	Solar radiation (insolation) inclination angle w.r.t. normal to the absorber plate of SAH ($^\circ$)

Abbreviation

BM	Bell-mouth
$CORR$	Chimney outlet to inlet radius ratio, R_{co}/R_{ci}
$CPSP$	Curved plate single pass flow solar air heater

<i>HSCPP</i>	Hybrid solar chimney power plant
<i>HTEF</i> or <i>EF</i>	Heat transfer enhancement factor ($Nu_{\text{curved}} / Nu_{\text{flat}}$)
<i>NuP</i>	Nusselt number per unit pressure drop ($Nu / \Delta P$)
<i>MER</i>	Mass flow rate enhancement ratio ($\dot{m}_{\text{tapered with BM}} / \dot{m}_{\text{flat plate conventional}}$)
<i>PV</i>	Photovoltaic
<i>SAH</i>	Solar air heater
<i>SCPP</i>	Solar chimney power plant
<i>TER</i>	Temperature enhancement ratio ($T_{o \text{ curved}} / T_{o \text{ flat}}$)
<i>TPP</i>	Total pressure potential, $N \text{ m}^{-2}$
<i>TR</i>	Collector taper ratio
<i>WSC</i>	Wedge shape collector

Abstract

The main focus of the PhD thesis has been to conceive and evaluate novel concept of bell-mouth and new collector design that can be easily integrated to solar energy devices such as solar chimney power plant (SCPP) and solar air heaters (SAH). Interestingly, both SCPP and SAH has common design components and work on the same natural convection principle. Both these devices have the following components: a solar collector and chimney. A novel concept of bell mouth inlet design, which reduces the losses significantly, has been developed and integrated to both SCPP and SAH and their thermal performance has been evaluated under various designs and environmental conditions.

Solar energy is a vast source of heat provided by the sun in the form of solar radiation, if utilized efficiently, can save millions of tons of carbon dioxide released by burning of fossil fuels. Sooner or later, the non-renewable sources of energy such as coal, diesel, petrol etc. would cease to exist due to excessive exploitation by human race. The only alternative would then be to develop efficient technologies to harness renewable sources of energy such as solar energy. Though solar energy is clean and available in abundance, it is not a concentrated source of energy like non-renewable sources of energy. One of the way to effectively use the solar radiant energy by redesigning of inefficient conventional solar energy powered devices. Among solar-thermal devices, solar chimney power plant (SCPP) is well known for electricity production and solar air heater (SAH) for air heating. Both works on the same principle: buoyancy driven mechanism. Though these clean energy powered systems are well established but their operational efficiency suffers owing to design limitations. A series of efficient novel designs of SCPP and SAH, with working fluid as air have been analyzed using experimentally validated CFD models. A combination of new concept of bell-mouth (BM) design inlet, converging collector flow channel and divergent chimney has significantly enhanced the power output by 9 folds. If multiple of such systems would be installed in the regions which are rich in sunshine, it can efficiently produce electricity to power almost thousands of villages. Further, this bell-mouth design was examined in conventional buoyancy-driven SAH with an objective to enhance the low hydraulic efficiency of the device. It was interesting to observe that the integration of bell-mouth design inlet significantly enhanced the mass flow rate of heated air. The high mass flow rates makes the device suitable for high flow rate applications. Secondly, the air temperature of the high flow SAH has been augmented by converging the parallel flow passage of SAH. Furthermore, a new convex and concave flow passage of naturally-driven SAH was designed and investigated for thermal performance. The energy and exergy analysis has been carried out for corrugated curved SAH. All the aforesaid new designs show significant impact in increasing the thermal and hydraulic performance of the solar-thermal devices. Lastly, a detailed aerodynamic analysis has been conducted to predict the real environmental wind impact on flat and curved SAH performance.

The chapter 2 explored the avenues to improve the electrical power output of conventional solar chimney power plant. As conventional sources of energy are depleting fast, solar energy based devices can only be mass adopted in future if suitable design innovations are conceptualized and investigated to improve its extremely low energy conversion efficiency. In this chapter, a series of new design concepts of solar chimney power plant are proposed and systematically investigated using an experimentally validated numerical model to maximize power generation capacity. A solar chimney consists two important components: a collector and a chimney. In a first, design of a third component called bell-mouth inlet with different orientation is proposed, investigated and optimized along with collector and chimney. Results show that with suitable design changes in collector, chimney and integrating an efficient bell-mouth at the inlet can increase the air velocity and hence turbine

output by about 270% compared to the conventional design. Physics behind such high increase in air velocity was also investigated. It is observed that total pressure potential or the static pressure recovery becomes high and uniform along the chimney height in the new design, which is entirely absent in conventional design. An uniform pressure distribution across the chimney height eliminates the recirculation zones thereby enhancing the system capacity to handle higher volume flow rates. Further analysis was conducted by scaling the lab-scale conventional model and proposed optimized design to a 50 kW power plant. Results show that the proposed new system can produce electrical power up to 1738 kW, which is about 35 times the conventional design can produce. The proposed design has the potential to meet the energy needs of thousands of villages.

The chapter 3 examines the possibility of integrating a photovoltaic (PV) module in a hybrid solar chimney power plant (HSCPP). Since HSCPP is a greenhouse thermal buoyancy-driven system, the surrounding high temperature environment makes PV module temperature extremely high resulting in lower electrical conversion efficiency. Various design configurations of collector duct and solar chimney are investigated using an experimentally validated numerical model to study the PV panel cooling and turbine power output. The results show that turbine power output is sensitive to diverging the chimney up to maximum static pressure recovery limit while PV module shows marginal increase in electrical efficiency. Converging the collector duct alone shows worst turbine and PV module performance. However, in case of combine designs of converging duct and divergent chimney, considerable improvement of PV panel efficiency (about 7%) was observed. The results show that about 80% of the collector area measured from the chimney axis are the most effective region for cooling the PV module where consistent temperature drop of 10-12 °C was observed. A design map vs. PV panel efficiency has been shown charting future directions for designing such energy efficient hybrid solar chimney systems.

Conventional natural convection flat plate solar air heater (SAH) suffers from low heat transfer characteristics. Putting extended surfaces in the air flow channel to augment thermal performance actually hinders the buoyancy driven flow, and thereby reducing the hydraulic performance due to high frictional losses. The objective of the chapter 4 is to enhance thermo-hydraulic performance by incorporating convex and concave flow channel with chimney effect. The curved SAH has been investigated using an experimentally validated computational fluid dynamic model for different curvature angles in the range of 25°-50°. The results show significant increase in Nusselt number per unit pressure drop (NuP), heat transfer enhancement factor, temperature enhancement ratio and effectiveness, in comparison to conventional flat SAH. The convex and concave designs are respectively 43% and 31% thermally, and 7% and 6% by NuP, higher than conventional flat natural convection SAH. Two different independent correlations derived for Nusselt number for different geometries were found to be in excellent agreement with the data. The designs and data presented in the study would help scientific community and solar based industries in developing efficient natural convection SAH.

Previous investigations have mainly focused on enhancing the thermal performance of a natural convection solar air heaters (SAH) at the expense of hydraulic performance by incorporating protruded surfaces and, thereby compromising on air mass flow rate significantly due to considerable pressure drop. Low mass flow rate of SAH makes it unsuitable for wide applications. In the chapter 5, design investigations using experimentally validated numerical model of SAH is reported that enhances flow rate by more than 100% in comparison to conventional flat plate SAH design. Integration of bell-shaped designs at the inlet of SAH adds to the ram-air effect that converts dynamic pressure into static pressure thereby manifesting into an excellent enhancement of air flow rate as well as in heat transfer associated with less hydraulic losses. The high-flow SAH was further investigated for building application using unsteady first-law of thermodynamic equation and it was observed to be 33% efficient over conventional design.

The bulk movement of fluid in natural convection solar air heater (SAH) is generated due to density variation and hence suffers from lower mass flow rates. Mounting additional surfaces/fins in SAH duct enhances the thermal characteristics, however, it comes at the cost of hydraulic performance. This limits the device usage in buildings and other high flow rate applications. In the chapter 6, two new designs of SAH were numerically analyzed are: (a) taper flow passage for better thermal performance; (b) tapered designs incorporated with bell-mouth inlet opening for improved hydraulic performance. Parametric design analysis was conducted for large range of taper ratio and bell-mouth ratio. The results show that the tapered design is about 70% thermally more effective and about 6% higher Nusselt number per unit pressure drop than conventional SAH. A significant enhancement in hydraulic performance of more than 300% was observed when bell-shaped inlet design was

integrated with the tapered designs.

In chapter 7, the investigation of various curved solar air heater designs has been reported. The promising design modifications proposed to further look for the avenues for thermal efficiency enhancement features. It was observed that secondary vortex formation near the absorber wall increases the Nusselt number significantly. New correlations for friction factor and Nusselt number has been developed as a function of Reynolds number and various geometric parameters such as relative groove height and pitch ratios for different design of air heaters. It is hoped that data of parameters i.e. Nusselt number (Nu), outlet air temperature (T_o), thermal efficiency (η_{th}) and friction factor (f) presented in this chapter would help researchers and industry in developing efficient designs of solar collectors.

Further, it has been observed that down-configurations of turbulators or extended surfaces on the flat plate solar collector significantly enhance the thermal performance. However, scientific literature on thermal performance investigations with down-configurations of ribs in curved SAH are rare. In the chapter 8, we systematically investigate using experimentally validated computational fluid dynamics model for different shapes of down-configuration of ribs. It was observed that half-trapezoidal and quarter-circular shape ribs shows maximum increase in thermal performance i.e. 17% and 16% , respectively, however frictional loss for quarter-circular ribs was observed to be less by about 10% when compared to trapezoidal shape ribs. The exergy recovery is maximum for trapezoidal and circular shape ribs and it is about 35% more than the smooth flat SAH. A new correlation has been developed for Nusselt number variation which has the form as $Nu = f [Re, \frac{e_r}{H}]$ where e_r is the height of quarter-circle groove. Observed data from the model matches well with the prediction from the developed correlation.

The chapter 9 evaluates and compares the performance matrix of a curved and flat solar air heater (SAH) under diverse environmental conditions using an experimentally validated numerical model. Firstly, the optimum curvature angle for curved SAH that offers optimum thermal performance (i.e. 25°) under wide range of parameters such as Reynolds numbers (2200 – 6000), mass flow rate (0.0172 – 0.0472 kg/sm²) and solar radiation inclination angle (0 – 60°) has been determined. The enhancement factor (i.e. Nu_{curved}/Nu_{flat}) is in the range 1.5 – 2.2 which show that curved SAH is thermally much better than flat design. Secondly, the optimized curved SAH is then compared with flat design for 0 to 60° tilt angles (θ), under tranquil and windy conditions (wind velocity range: 0.5 – 4 m/s), respectively. Under windy condition the heat loss from SAH to surrounding is lower for curved SAH at $\theta = 0^\circ, 60^\circ$ in windward, 30° in leeward and 30° in tranquil- condition in comparison to flat SAH. In the extreme case $\theta = 60^\circ$ and wind speed of 4 m/s, , the percentage change in average differential pressure coefficient ΔC_p is about 2% higher for curved SAH under windward while it is about 19% less in leeward condition compared to flat SAH.

A series of novel designs of solar-thermal devices have been investigated in the thesis with an objective to maximize the energy conversion for useful work. The efforts put in the present research is a small step towards the theme of '*Let's go green to get our globe clean*'.

